Computers in Biology and Medicine 198 (2025) 111138

Contents lists available at ScienceDirect

Computers in Biology and Medicine

journal homepage: www.elsevier.com/locate/compbiomed

Prediction of fast subcellular calcium signals based on label-free second harmonic generation microscopy measurements

Tihomir Georgiev

Department of Experimental Ophthalmology, University Hospital Cologne, University of Cologne, Cologne, Germany

A B S T R A C T

Calcium (Ca^{2+}) sparks were predicted based on the label-free second harmonic generation (SHG) signal of myosin filaments with pix2pix, a conditional adversarial network. Predicted Ca^{2+} sparks and ground truth Ca^{2+} sparks show similar properties. Predicted Ca^{2+} spark frequencies and a predominant location at the periphery of skeletal muscle fibers were in good agreement with ground truth data. High frequencies of predicted Ca^{2+} sparks could be observed at y-shaped structures of myosin filaments. Important image pre-processing was applied in order to enhance the signal of Ca^{2+} sparks used for training. Only open-source software was applied. I provide the image pre-processing algorithm and several algorithms to evaluate the quality of predicted Ca^{2+} sparks. This technique can be extended to other label-free microscopy techniques and other fluorescent indicators developed during the last years. It remains a difficult task to predict the exact location of Ca^{2+} sparks.

1. Introduction

Ca^{2+} is an important intracellular signal [1]. Ca^{2+} sparks are fast and small Ca^{2+} signals in different cell types [2,3]. I use the term Ca^{2+} sparks to describe localized Ca^{2+} signals in skeletal muscle fibers (Ca^{2+} sparks and Ca^{2+} bursts as defined in a previous publication [4]). High frequencies of Ca^{2+} sparks can be observed in permeabilized skeletal muscle fibers [5] and during an osmotic treatment in intact skeletal muscle fibers [4]. Machine learning has been applied for the analysis of Ca^{2+} signals recently [6–12]. Generative adversarial networks have been introduced by Goodfellow et al. [13] and have been applied for segmentation of Ca^{2+} signals [14]. Recently, machine learning has been applied for segmentation and classification of Ca^{2+} sparks [15–17]. Additionally, T cell classification based on intracellular calcium signals has been carried out using machine learning predictions [18].

In light microscopy, in silico labelling of subcellular structures based on bright field images has been achieved with deep learning [19,20]. Image translations of medical images have been generated with deep learning for different applications such as synthesis of post contrast MRI images [21] or translation of MRI images to PET images [22].

To my knowledge, this paper is the first attempt to translate structural images to images of Ca^{2+} signals. Second harmonic generation (SHG) microscopy is a nonlinear optical microscopy technique that allows the label-free visualization of myosin filaments in skeletal muscle fibers [23,24]. In vivo SHG measurements have been described in a previous study [25]. Localized Ca^{2+} signals have been investigated with respect to the myosin filaments in striated muscle cells previously [26,27]. In this study, I used the SHG signal of myosin filaments as subcellular structural information to generate synthetic images of Ca^{2+} signals (predicted Ca^{2+} sparks). The training of the network was carried out on pairs of images consisting of an SHG measurement and a two photon microscopy [28] measurement of Ca^{2+} sparks in skeletal muscle fibers. Different strategies have been applied to translate images previously [29,30]. I applied the pix2pix algorithm [30] for the translation of images which is based on conditional adversarial networks. The prediction of Ca^{2+} sparks based on subcellular structures is a difficult task since the exact location of Ca^{2+} sparks is difficult to predict. Additionally, Ca^{2+} sparks are small and fast subcellular signals in a noisy cellular environment.

Changes of the amplitude of Ca^{2+} bursts have been shown in skeletal muscle fibers of *mdx* mice, as a model for dystrophic muscle, compared to skeletal muscle fibers of wild type mice [4]. Additionally, a predominant location of Ca^{2+} sparks at the periphery of skeletal muscle fibers of wild type mice has been described [4]. Y-shaped structures can be found more frequently in skeletal muscle fibers of mdx mice compared to wild type mice [31]. High frequency of Ca^{2+} sparks has been observed at y-shaped structures [26]. Differences in the amplitude and size of Ca^{2+} sparks have been observed under different conditions in mdx mice [32]. Therefore, I investigated such properties of predicted Ca^{2+} sparks.

Changes in the SHG signal depending on different conformations of myosin molecules have been described in skeletal muscle fibers and myofibrils [33–35]. An increase of the SHG signal in skeletal muscle fibers has been shown after an increase of the intracellular Ca^{2+}

E-mail addresses: tihomir.georgiev@mail.de, tgeorgi1@smail.uni-koeln.de, tihomir.georgiev@uk-koeln.de.

https://doi.org/10.1016/j.compbiomed.2025.111138
Received 5 May 2025; Received in revised form 15 September 2025; Accepted 22 September 2025
Available online 27 September 2025

concentration [35]. Additionally, localized sarcomere contractions could be observed in response to Ca^{2+} sparks in cardiac muscle cells [27]. Therefore, I investigated possible subcellular changes of the SHG signal at regions of Ca^{2+} sparks.

2. Methods

2.1. Data

The SHG images and two photon microscopy images used to train and test the algorithm were measured simultaneously in a previous publication [26].

Wild type mice (C57BL) were sacrificed according to local animal care committee guidelines [26]. Briefly, skeletal muscle fibers were enzymatically isolated from the interossei muscles of the toe and measurements were carried out on the same day [26,36]. An isotonic solution (mmol/l): NaCl 140, KCl 5, $CaCl_2$ 2.5, $MgCl_2$ 2, HEPES 10, pH 7.2 [4] was used for isolation and staining of the fibers [26]. During measurements of Ca^{2+} sparks a hypertonic solution was applied (mmol/l): NaCl 140, KCl 5, $CaCl_2$ 50, $MgCl_2$ 2, HEPES 10, pH 7.2 [4,26]. Muscle fibers were stained with the fluorescent Ca^{2+} indicator Fluo-4 AM (Life technologies, Molecular Probes, Eugene, OR, USA) for 30 min at 37 °C and placed on poly-lysine coated coverslips (Sigma-Aldrich, St. Louis, MO, USA) [26]. After the addition of the hypertonic solution measurements were performed within 70 min [26].

The optical setup for SHG measurements and two photon microscopy measurements of ground truth Ca^{2+} sparks used to train and test the network has been described previously [23,26]. The optical system consists of a modified inverted microscope (DM IRBE, Leica Microsystems, Mannheim, Germany), a confocal laser scanning unit (SP2 MP, Leica), two 63× water immersion objectives (PL APO 63×/1.20 W CORR, Leica) and a pulsed Ti:Sa-based laser (Tsunami, Spectra Physics, Irvine, CA, USA) with a pulse length of approximately 2 ps [26]. The central wavelength was tuned to approximately 880 nm and the average laser power at the back aperture of the objective was 150 mW–190 mW [26,35].

SHG signal was measured on the transmitted light path using a photomultiplier tube (R6357, Hamamatsu, Hamamatsu City, Japan) [26]. An IR block filter and band pass filters (centered at approximately 440 nm, pass band approximately 20 nm) were placed in front of the photomultiplier tube in order to exclude the laser beam and two photon excited fluorescence signal [26].

For the measurement of two photon excited fluorescence of Ca^{2+} sparks a non-descanned photomultiplier tube (R9624, Hamamatsu) in the reflected light path was used [26]. Laser light was blocked with a beam splitter and a short pass filter (wavelength <650 nm) [26]. Additionally, fluorescence and SHG signal were separated using a second beam splitter so that photons above a wavelength of approximately 480 nm were measured [26]. Measurements are xyt 8-bit images with an image size of 512 by 512 pixels and a pixel size of 233 nm [26]. Each image was measured in 0.64 s and the time difference between measurements is 0.18 s [26].

Skeletal muscle fibers were measured randomly oriented on coverslips.

2.2. Image pre-processing

The first step of the image pre-processing was to automatically identify Ca^{2+} sparks. Similar ideas for automatic detection of Ca^{2+} sparks have been described in previous publications [37,38]. First, a 2D gaussian filter with a standard deviation sigma = 2 was applied on each image of the xyt measurement. Then, based on the gaussian signal image the mean intensity was calculated along the t axis, a binary image was generated using the mean image with a threshold of $2*\sigma$, with σ the standard deviation. Different objects of the binary image were labelled and objects smaller than 3000 pixels were excluded since in some images fluorescent parts of damaged cells outside the fiber could be observed. The area of 3000 pixels (163 μm^2) is much smaller than the fiber areas shown in the images. Then, a binary fiber mask was created. To exclude labelled structures outside the fiber, the Ca^{2+} measurement after application of a gaussian filter was multiplicated by the cleaned binary fiber mask. Binary image that includes the Ca^{2+} sparks was generated. Pixels were assigned a value of 1 if their value is higher than $\mu + 3.6*\sigma$, with μ the mean fluorescence intensity within the fiber and σ the corresponding standard deviation. μ and σ were measured within the fiber mask. Then objects of the binary images were labelled and objects smaller than 55 pixels were excluded. Assuming Ca^{2+} sparks are circles, the smallest possible Ca^{2+} sparks in this study have a radius of <1 μm. Such small objects were excluded since in some fibers small intracellular structures with strong fluorescence intensity were seen in all images of the xyt measurement. Additionally, this criterion was applied to avoid the detection of noise. Then again, a binary image of Ca^{2+} sparks was created based on the cleaned labelled image.

Finally, the Ca^{2+} sparks in the original image were enhanced 10 times compared to the fiber background by reducing the fiber background 10 times. This step was important in order to make it easier for the network to see the Ca^{2+} sparks.

2.3. Translation of Ca^{2+} sparks based on SHG images

19 measurements of 4 fibers from two mice were used to train the algorithm. The training was carried out with 4123 images containing 256x256 pixels with 818 Ca^{2+} sparks. Thereby, 1031 images containing 512x512 pixels were cropped to 4123 256x256 pixel images so that the image size is compatible with the input of the network.

To test the performance of the trained network, three different experiments Exp 1 (experiment 1), Exp 2 (experiment 2), Exp 3 (experiment 3) were carried out.

The experiments were designed in order to test predictions of the Ca^{2+} signalling pattern based on SHG measurements of skeletal muscle fibers unseen during training (Exp 1) and of a muscle fiber that was included in the training data set but at a different plane (Exp 2). In Exp 3, I tested how well the signalling pattern in the future and past of a specific plane in a skeletal muscle can be predicted.

Exp 1 consists of 545 512x512 pixel images from 5 measurements of two fibers from two mice (the same animals as used for training but different fibers), which were not included in the training data. 683 ground truth Ca^{2+} sparks are included in this data set. The rationale behind Exp 1 is to predict Ca^{2+} sparks based on the SHG signal of the fiber without staining with Ca^{2+} indicators.

Exp 2 consists of 196 512x512 pixel images from 4 measurements of a fiber that was included in the training data but showing a different plane. This data set contains 292 ground truth Ca^{2+} sparks. The plane is at the periphery of the fiber. The plane of the fiber included in the training data set is at the center of the fiber. It is expected that the plane included in Exp 2 shows higher frequency of Ca^{2+} sparks compared to the training data set of this fiber [4]. The rationale behind this experiment is to see if such difficult predictions are better than predictions of unseen fibers during training.

Exp 3 consists of 98 512x512 pixel images from two measurements of a fiber. Different measurements of this muscle fiber were included at the same plane in the training data. One measurement was carried out before and one after the training data set of this fiber. The data set contains 102 ground truth Ca^{2+} sparks. The rationale behind Exp 3 is that such predictions are expected to be easier than predictions of Exp 1. Additionally, with such predictions it might be able to predict the Ca^{2+} signalling pattern in past and future measurements based on the myosin filament pattern at a specific time point.

Fibers were selected if they showed clear Ca^{2+} sparks activity and a band pass filter was placed in the SHG signal detection path [26] and no or little shift of the muscle fiber was observed during measurement. Additionally, 2 measurements were included in Exp 1 without a band

pass filter in front of the SHG detector in order to test if a contamination of the SHG signal by two photon excited fluorescence influences the prediction of Ca^{2+} sparks.

Since there is a high variability of Ca^{2+} sparks signalling patterns and because no augmentation was carried out during the training process, images in Exp 1 and Exp 2 were rotated at 90°, 180°, 270° and 360°. Therefore, the algorithm was tested on 2180 512x512 pixel images in Exp1 and 784 512x512 pixel images in Exp 2.

All images in the three experiments were cropped to 256x256 pixel images as input for the image translation algorithm.

In Exp 1 and in Exp 2 for the four angles 2307 and 702 Ca^{2+} sparks were predicted respectively. In Exp 3103 Ca^{2+} sparks were predicted.

Additional analysis was carried out for Exp 1 (Fig. 5 and Extended Data Fig. 11). Exp 1 was divided in three different data sets. Exp 1 GT 1nf is the ground truth data set of fiber 1 without a band pass filter in front of the SHG signal detector. Exp 1 GT 1nf consists of 401 ground truth Ca^{2+} sparks. Exp 1 P 1nf are the predicted images of Exp 1 GT 1nf with 1628 Ca^{2+} sparks after rotation of images with 4 different angles as input. Exp 1 GT 1 is the ground truth data set of fiber 1 with a band pass filter in front of the SHG signal detector. This data set contains 90 Ca^{2+} sparks. The corresponding prediction Exp 1 P 1 for 4 rotations contains 155 Ca^{2+} sparks. Exp 1 GT 2 is the ground truth data set of fiber 2 from another mouse and contains 192 Ca^{2+} sparks. The corresponding prediction for 4 rotations contains 524 Ca^{2+} sparks.

The code for image translations was taken with minor modifications from https://www.tensorflow.org/tutorials/generative/pix2pix and is based on the publication of Isola et al. [30]. The structure of the network was not modified. The network was trained for 35 epochs, batch size of 1.

2.4. Analysis of translated images

As first analysis step of the translated images, fiber masks of the ground truth and predicted Ca^{2+} signal were generated in order to determine the fiber area and the mean fluorescence intensity within the fiber. First, a 2D gaussian filter with a standard deviation sigma = 2 was applied on the Ca^{2+} images. Then, a binary image of the mask was created. Pixels were assigned the value 1 if their value was higher than a criterion based on σ the standard deviation of the corresponding image. In the enhanced ground truth Ca^{2+} image the Ca^{2+} signal outside the fiber was set to 0 as described previously in the image pre-processing part. In the predicted Ca^{2+} images some pixels with values higher than 0 could be rarely observed outside the fiber. To exclude these pixels, objects in the binary images satisfying a condition based on σ were labelled. Then, objects smaller than 3000 pixels were excluded and a cleaned binary image was generated.

Predicted Ca^{2+} sparks were automatically identified as described in the image pre-processing section but with fiber masks generated as described in this section (analysis of translated images) since predicted images might show some variability of the generated fibers. Properties of Ca^{2+} sparks (Ca^{2+} spark area, Ca^{2+} spark mean fluorescence intensity and the ratio Ca^{2+} spark area/Ca^{2+} sparks edges) were determined based on the labelled binary images of Ca^{2+} sparks. Ca^{2+} spark frequencies (densities) were defined as the following ratio: number of Ca^{2+} sparks in an experiment/total fiber mask area in an experiment. Additionally, I calculated means and standard deviations (SD) of the Ca^{2+} sparks frequencies (densities) image-wise. Thereby, the Ca^{2+} sparks frequencies for every image of Exp 1, Exp 2 and Exp 3 were determined as number of Ca^{2+} sparks in an image/fiber mask area of the image. Then, I calculated means and SD for Exp 1, Exp 2 and Exp 3.

An algorithm was developed to automatically detect the fiber periphery. First, the border of the image was detected using ndi.binary_delation of scipy. Then, pixels touching the image border and being part of the fiber mask were assigned a value of 1. Then, using a fiber erosion (ndi.binary_erosion of scipy) over 40 steps an image was iteratively created that shows the centre of the fiber. On each of the 40 steps the images with pixels assigned a value 1 when touching the image border and being part of the fiber mask were added to the eroded image in order to avoid the centre of the fiber touching the image border being assigned to the fiber border (512x512 pixel images Fig. 3a and b). With this eroded image and the fiber mask image an image of the fiber periphery was created. If there were overlapping pixels of the fiber periphery and the binary image of Ca^{2+} sparks, the Ca^{2+} spark was counted as a signal at the fiber periphery.

For the measurement of the Ca^{2+} spark area over myosin filaments, the mean SHG signal over the whole measurement was used. First, a 2D gaussian filter with a standard deviation sigma = 2 was applied on the mean SHG signal. Then, a fiber mask was generated with pixels assigned the value 1 if they fulfil the condition > σ, with σ the standard deviation of the mean SHG signal. To create a binary image of the myosin filaments the module filters.rank.mean of scikit image was applied on the mean SHG signal with a disk size of 5. The images of the mean SHG signal were multiplied by the fiber mask. The Ca^{2+} spark area over the myosin filaments was calculated based on the binary image of the mean SHG signal and the labelled binary image of Ca^{2+} sparks.

Y-shaped structures were manually annotated on mean SHG measurements using Fiji [39]. With these binary images of y-shaped structures and the labelled binary images of Ca^{2+} sparks, the Ca^{2+} spark area over y-shaped structures was calculated. If 30 % of the Ca^{2+} spark area overlaid y-shaped structures, it was counted as Ca^{2+} spark at y-shaped structures and the corresponding Ca^{2+} spark frequencies at y-shaped structures were calculated for the three experiments with the corresponding areas of y-shaped structures. The frequency of Ca^{2+} sparks at y-shaped structures was calculated experiment-wise as the total number of Ca^{2+} sparks at y-shaped structures for all images of an experiment divided by the total area of y-shaped structures for all images of an experiment. I also calculated Ca^{2+} spark frequencies at y-shaped structures image-wise for Exp 1, Exp 2 and Exp 3. The frequency of Ca^{2+} sparks at y-shaped structures of an image was calculated as number of Ca^{2+} sparks at y-shaped structures of the image divided by the area of y-shaped structures of the image. Then the mean and standard deviation for all images in an experiment was calculated. In this case, there were many images with no Ca^{2+} sparks at y-shaped structures and images with high frequencies of Ca^{2+} sparks at y-shaped structures because of the small area of y-shaped structures.

The ratios SHG signal (spark)/SHG signal (fiber) and Calcium signal (spark)/Calcium signal (fiber) in Fig. 5 are the mean SHG signal or Ca^{2+} signal at the region of a Ca^{2+} spark divided by the mean SHG signal or mean Ca^{2+} signal of the fiber mask when regions of Ca^{2+} sparks were excluded from the fiber mask.

The ratios SHG signal (spark)/SHG signal (measurement) and Calcium signal (spark)/Calcium signal (measurement) are the SHG signal and Ca^{2+} signal at the Ca^{2+} spark region divided by the mean SHG signal or mean Ca^{2+} signal over 49 or 50 images at the same region. Measurements were selected for analysis, if they showed no or negligible fiber shifts.

2.5. Statistics

Pearson correlation coefficients and linear regression were calculated with Scipy [40], Matthews correlation coefficients were calculated with Scikit learn [41], structural similarity index (SSIM) [42] and mean squared error [43] (SME) were calculated with Scikit image [44]. Violin plots and box plots were plotted with Matplotlib [45]. Boxes in boxplots extend from Q1 to Q3 (with Q1 lower quartile and Q3 upper quartile), median is indicated by the horizontal line, triangles indicate means, upper and lower whiskers show last data point less than Q3 + 1.5* (Q3-Q1) and first data point greater than Q1- 1.5 (Q3-Q1) with (Q3-Q1) the interquartile range and the circles indicate datapoints beyond the whiskers [45]. The F1 score was calculated as described by Moen et al. [46]. P values were calculated using a Mann-Whitney *U* test with Scipy [40].

2.6. Software

The following software was used in this paper: Python, Jupyter, Spyder, Tensorflow [47], Tensorflow_io, Keras [48], Scikit learn [41], Scikit image [44], Numpy [49], Matplotlib [45], Scipy [40], Tifffile [50], Os, Pathlib, Time, Datetime, IPython [51], Xlsxwriter, ImageJ [52], Fiji [39], ChimeraX [53], https://www.tensorflow.org/tutorials/generative/pix2pix and https://github.com/embl-bio-it/image-analysis-with-python/blob/master/session-3to5/image_analysis_tutorial_solutions.ipynb.

3. Results

3.1. Generation of translated images

As a first step, Ca^{2+} sparks were enhanced compared to the background signal of the cell (Fig. 1a). Then, the network was trained on pairs of SHG images and enhanced Ca^{2+} images (Fig. 1b). The trained network was then applied to translate Ca^{2+} images based on SHG images (Fig. 1c). Fig. 1c shows only one Ca^{2+} spark in the translated image. Some translated Ca^{2+} sparks could be seen on every image of the measurement. Other translated Ca^{2+} sparks appeared only on some images of the measurement (Extended Data Fig. 1b, c, f). On several translated images two, three or four Ca^{2+} sparks could be observed (Extended Data Fig. 1a, b, c, f). Ca^{2+} sparks could be found at subcellular structures of the myosin pattern, so called y-shaped structures (Fig. 1d).

I tested the performance of the trained network on three different experiments Exp 1 (experiment 1), Exp 2 (experiment 2), Exp 3 (experiment 3). In Exp 1 measurements of fibers were translated that were not included in the training data. Measurements showing a plane of a skeletal muscle fiber unseen during training were translated in Exp 2. However, measurements of another plane of this fiber (Exp 2) were included in the training data. Exp 3 contains two measurements of a different fiber. Other measurements of the same plane of this fiber were included in the training data.

Structural similarity index (SSIM) [42] and mean squared error (SME) [43] were calculated (Fig. 1e and f). The translated images achieved high SSIM values. Mean values and standard deviation of SSIM and SME when analysed image-wise can be found in Extended Data Fig. 2a and b.

3.2. Properties of translated Ca^{2+} images

As a next step, I investigated several properties of translated images. The fiber masks of ground truth and predicted images were similar (Fig. 2a, b, c and d). The mean fiber intensity was lower in the predicted images, this was particularly the case in experiment 1 (Exp 1) (Fig. 2e). However, the mean of the fiber mean fluorescence intensity in the ground truth data of Exp 1 was higher than in the other two experiments and in the training data set.

Then, I investigated the properties of predicted Ca^{2+} sparks compared to ground truth Ca^{2+} sparks. I found that predicted Ca^{2+} spark area in Exp 1 was in good agreement with ground truth Ca^{2+} spark area (Fig. 2f). Interestingly, larger differences could be observed for the other two experiments. The predicted spark mean intensity was lower in all experiments (Fig. 2g). This was most pronounced in Exp 1. Standard deviations of fiber area, fiber mean intensity, spark area and spark mean intensity are shown in Extended Data Fig. 3. The predicted ratio Ca^{2+} spark area/Ca^{2+} spark edge was larger than this ratio in the ground truth data for all experiments suggesting that predicted Ca^{2+} sparks are more circular (Fig. 2h).

The predicted Ca^{2+} spark frequency in Exp 1 of 2.52 sparks/(10,000*μm^2) was in good agreement with the ground truth Ca^{2+} spark frequency of 3.05 sparks/(10,000*μm^2) (Fig. 2i). The predicted Ca^{2+} spark frequency in experiment 3 (Exp 3) of 2.78 sparks/(10,000*μm^2) was even closer to the corresponding ground truth Ca^{2+} spark frequency of 2.74 sparks/(10,000*μm^2). The training data set had a Ca^{2+} spark frequency of 1.85 sparks/(10,000*μm^2). However, there was a larger difference in experiment 2 (Exp 2) between the predicted Ca^{2+} spark frequency of 2.46 sparks/(10,000*μm^2) and the ground truth Ca^{2+} spark frequency of 4.36 sparks/(10,000*μm^2).

Additionally, I analysed the Ca^{2+} spark frequencies image-wise (Extended Data Fig. 2c): Exp 1 GT: (3.01 ± 2.42) sparks/(10,000*μm^2) (mean ± SD), Exp 1 P: (2.50 ± 2.26) sparks/(10,000*μm^2), Exp 2 GT: (4.37 ± 2.35) sparks/(10,000*μm^2), Exp 2 P: (2.43 ± 2.36) sparks/(10,000*μm^2), Exp 3 GT: (2.76 ± 2.01) sparks/(10,000*μm^2), Exp 3 P: (2.78 ± 0.59) sparks/(10,000*μm^2) (Extended Data Fig. 2c).

3.3. Translation of subcellular structures to fast subcellular signals

As a next step, I investigated specific subcellular regions of the muscle fiber known to have high frequencies of Ca^{2+} sparks, the fiber periphery [4] and y-shaped structures of the myosin pattern [26]. Additionally, I investigated the ratio Ca^{2+} spark area over myosin filaments/spark area.

As expected, most of the predicted and ground truth Ca^{2+} sparks were located at the fiber periphery (Fig. 3a, b, and c). The ground truth Ca^{2+} spark frequency at the fiber periphery in Exp 1 showed a lower fraction of Ca^{2+} sparks compared to the predicted fraction. This difference can be also seen in the ratio Ca^{2+} spark area over fiber periphery/spark area (Extended Data Fig. 5b). One of the fibers used in Exp 1 showed a high frequency of Ca^{2+} sparks in the centre of the fiber not seen for the other five fibers (Extended Data Fig. 4). Interestingly, predicted images of this fiber showed several Ca^{2+} sparks in the fiber centre in close proximity to the ground truth Ca^{2+} sparks but not at such high frequencies (Extended Data Fig. 4). If this fiber was excluded from the analysis, there is a good agreement between ground truth data and predicted data (Extended Data Fig. 5a).

Then, I looked at the ratio Ca^{2+} spark area over myosin filaments/spark area (Fig. 3d and e) and found that this ratio was lower for predictions. Several predicted Ca^{2+} sparks were located at regions without myosin filaments (Exp 1 P and Exp 2 P). Such Ca^{2+} sparks at myosin free regions can be found in the training data set.

As a next step, I investigated the translation of y-shaped structures of the myosin filament pattern to Ca^{2+} sparks (Fig. 3f, g and h and Extended Data Fig. 6). In Exp 1, the predicted Ca^{2+} spark frequency at y-shaped structures of 7.94 sparks/(10,000*μm^2) was 1.26 times higher than the ground truth Ca^{2+} spark frequency at y-shaped structures of 6.31 sparks/(10,000*μm^2). In Exp 2, no Ca^{2+} sparks were predicted at y-shaped structures while ground truth Ca^{2+} frequency at y-shaped structures was 3.92 sparks/(10,000*μm^2). In Exp 3, the predicted Ca^{2+} spark frequency at y-shaped structures of 13.93 sparks/(10,000*μm^2) was 1.56 times higher than the ground truth Ca^{2+} spark frequency at y-shaped structures of 8.95 sparks/(10,000*μm^2). When Ca^{2+} spark frequencies at y-shaped structures were analysed image-wise, I received the following values: Exp 1 GT: mean: 7.38 sparks/(10,000*μm^2), SD: 20.63 sparks/(10,000*μm^2); Exp 1 P: mean: 6.04 sparks/(10,000*μm^2), SD: 12.43 sparks/(10,000*μm^2); Exp 2 GT: mean: 3.89 sparks/(10,000*μm^2), SD: 14.06 sparks/(10,000*μm^2); Exp 2 P: mean: 0 sparks/(10,000*μm^2), SD: 0 sparks/(10,000*μm^2); Exp 3 GT: mean: 8.95 sparks/(10,000*μm^2), SD: 8.01 sparks/(10,000*μm^2); Exp 3 P: mean: 13.93 sparks/(10,000*μm^2), SD: 0.05 sparks/(10,000*μm^2).

Additionally, the ratios of SHG mean intensity at y-shaped structures and SHG mean intensity of the fiber based on the Ca^{2+} signal fiber mask were calculated image-wise for the three experiments: Exp 1: 0.9994 ± 0.0048 (mean ± SD), Exp 2: 0.9994 ± 0.0060, Exp 3: 1.0000 ± 0.0031.

3.4. Accuracy of Ca^{2+} spark prediction

Predicted Ca^{2+} sparks seen in all image translations of a measurement were several times associated with high ground truth Ca^{2+} spark

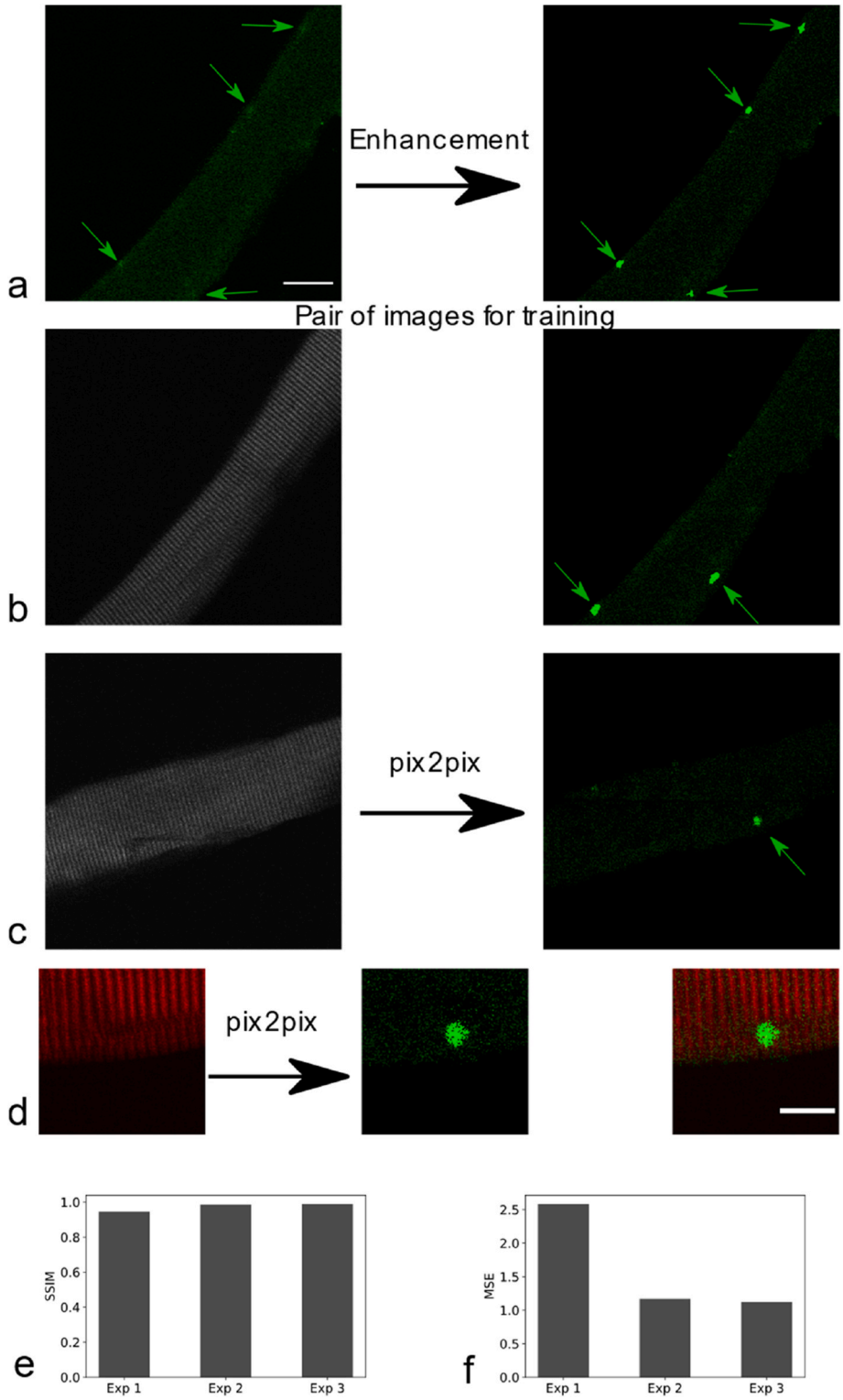

Fig. 1. ***Generation of translated images.*** ***a****, Pre-processing of* Ca^{2+} *sparks with enhancement of* Ca^{2+} *sparks compared to the background signal of the fiber. On the left side* Ca^{2+} *sparks (arrows) without enhancement are shown. On the right side* Ca^{2+} *sparks after enhancement can be seen. Scale bar* 20 μm ***b****, Pairs of simultaneously measured SHG signal of the muscle fiber (left) and enhanced* Ca^{2+} *sparks (arrows right image) used to train the network.* ***c****, The trained network was applied to translate SHG images to* Ca^{2+} *images. The arrow indicates a* Ca^{2+} *spark in the translated image. Measurements of this fiber were not included in the training data set (Exp 1).* ***d****, Translation of SHG signal (red signal, left) to* Ca^{2+} *signal (green signal, centre) with the trained network. Overlay of both signals (right). Y-shaped structures can be seen in the SHG measurement (average of 5 images). Other measurements of this fiber and this plane were included in the training data set (Exp 3). Scale bar* 10 μm. ***e*** *and* ***f****, Structural similarity index (SSIM) and mean squared error (MSE) of the three experiments used to test the performance of the trained network.*

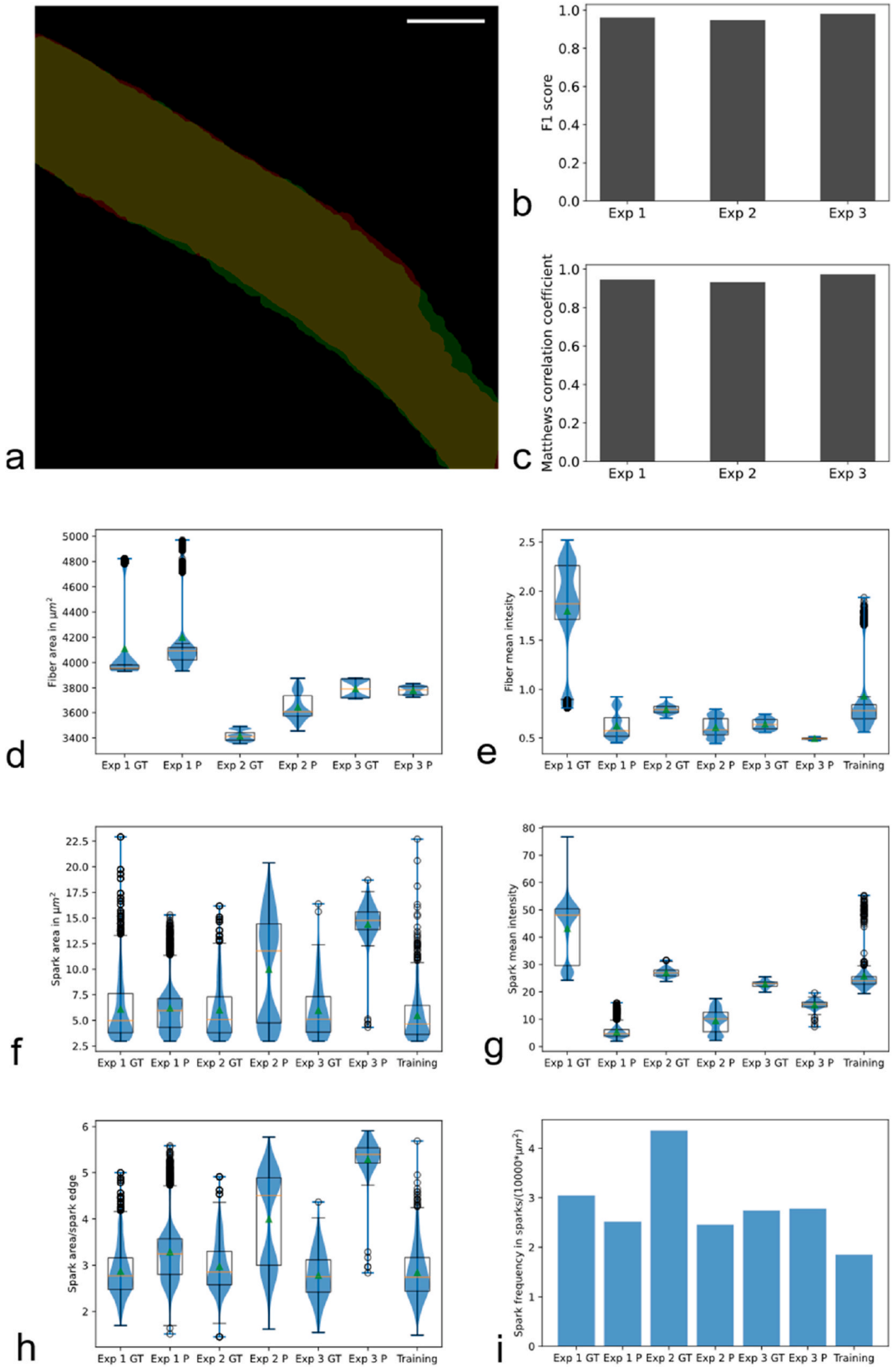

Fig. 2. Properties of translated images of Ca^{2+} sparks. a, Ground truth (red) and predicted (green) fiber mask of a fiber unseen during training of the network (Exp 1). The overlay of both masks is yellow. Scale bar 20 µm **b** and **c**, F1 scores and Matthews correlation coefficients for the evaluation of predicted fiber masks for the three experiments. **d**, **e**, **f**, **g** and **h**, Box plots and violin plots of the fiber area, fiber mean intensity, spark area, spark mean intensity and spark area/spark edge of the ground truth (Exp GT) and predicted (Exp P) images in the three experiments and the training data set. Orange lines are the medians of the data and green triangles are the means. **i**, Ca^{2+} spark frequencies of the ground truth and predicted images of the three experiments and the training data set.

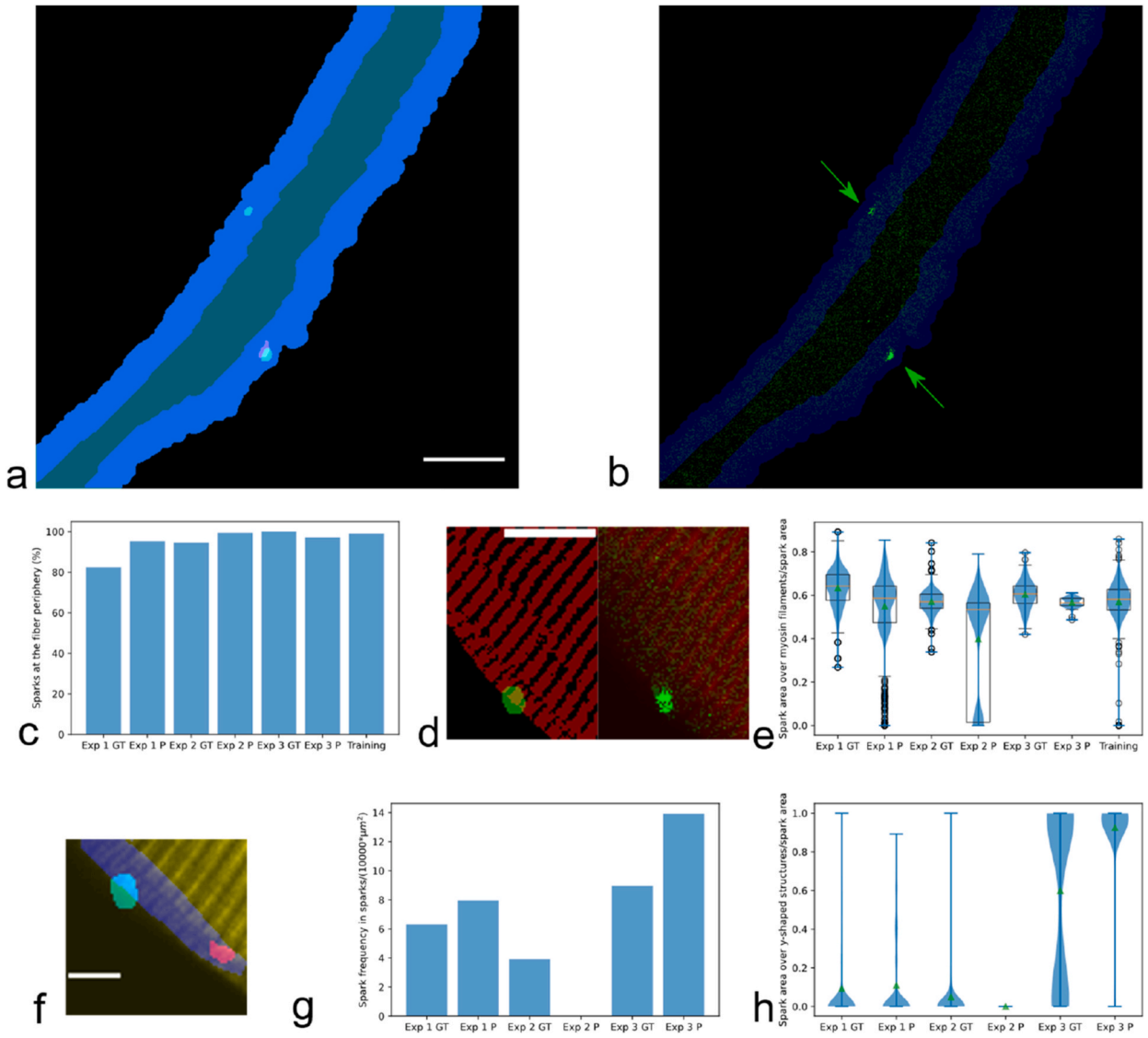

Fig. 3. Translation of subcellular structures to fast subcellular signals. a, Binary images of the fiber centre (cyan), periphery of the fiber (blue) and Ca^{2+} sparks (green) based on a predicted Ca^{2+} image of a fiber unseen during training of the algorithm (Exp 1). Additionally, a binary image of a Ca^{2+} spark measured in the ground truth image is presented (red). Scale bar 20 µm **b**, Overlay of the predicted Ca^{2+} signal (green) of the fiber shown in **a** and fiber periphery (blue). The arrows indicate Ca^{2+} sparks. **c**, Percentage of Ca^{2+} sparks at the fiber periphery for ground truth (Exp GT) and predicted (Exp P) images in the three experiments and the training data set. **d**, Overlay of binary images (left) of the myosin filaments (red) and a predicted Ca^{2+} spark. The binary SHG signal is based on a mean SHG signal of the whole measurement. Overlay of the mean SHG signal of the whole measurement (red) and the predicted Ca^{2+} signal (green) of the same image (right). This fiber was unseen during the training process of the algorithm (Exp 1). Scale bar 10 µm. **e**, Box plots and violin plots of the ratios of the Ca^{2+} spark area over myosin filaments and the Ca^{2+} spark area for ground truth (Exp GT) and predicted (Exp P) images in the three experiments and the training data set. Orange lines are the medians of the data and green triangles are the means. **f**, Overlay of the mean SHG signal during the whole measurement (yellow), mask of y-shaped structures (blue), binary image of a predicted Ca^{2+} spark (green) and binary image of a ground truth Ca^{2+} spark (red). The fiber was unseen during the training process (Exp 1). Scale bar 5 µm **g**, Ca^{2+} spark frequencies at y-shaped structures for ground truth (Exp GT) and predicted (Exp P) images in the three experiments. **h**, Violin plots of Ca^{2+} spark area over y-shaped structures/Ca^{2+} spark area for ground truth (Exp GT) and predicted (Exp P) images in the three experiments. Green triangles are the means.

activity in close proximity (Fig. 4a, b, c and d, Extended Data Movie 1 and 2). The predicted and ground truth Ca^{2+} sparks partly overlapped in these cases. However, the exact overlap was not high. This is reflected in low Pearson correlation coefficients, Matthews correlation coefficients and F1 scores (Fig. 4 e, f, g). Predicted Ca^{2+} sparks seen in all image translations of a measurement were often in close proximity or at y-shaped structures of the myosin filaments (Extended Data Fig. 7).

Extended Data Figs. 8 and 9 present the results when only one fiber was included in Exp 1.

3.5. Does the algorithm translate subcellular structures or signals?

To investigate possible subcellular changes of the SHG signal at regions of Ca^{2+} sparks, I analysed if there is such correlation (Fig. 5a, b and c). If there are Ca^{2+} dependent changes of the SHG signal, it is possible that the algorithm translates localized signals in SHG images to localized signals in Ca^{2+} images. The Pearson correlation coefficients for the different experiments are: Exp 1 GT 1nf: 0.0727, Exp 1 P 1nf: -0.4127, Exp 1 GT 1: -0.2998, Exp 1 P 1: -0.4564, Exp 1 GT 2: 0.0818, Exp 1 P 2: 0.6419, Exp 2 GT: 0.0299, Exp 2 P: -0.4498, Exp 3 GT: -0.1464, Exp 3 P: -0.4887, Training: -0.1896.

Interestingly, Exp 1 P 1nf shows negative Pearson correlation for the

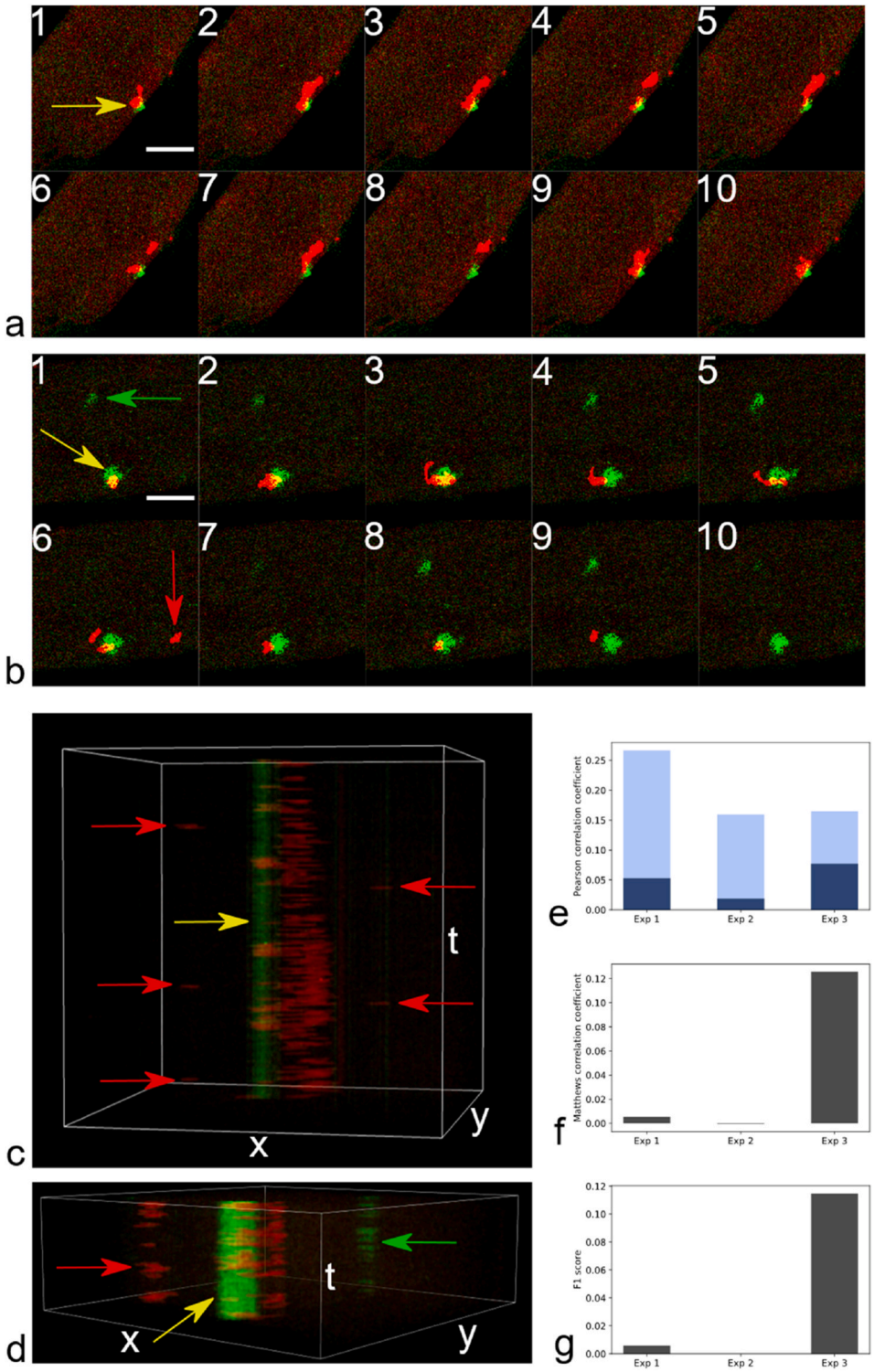

Fig. 4. Accuracy of Ca^{2+} spark prediction. a, Image sequence (10 consecutive images) of the ground truth Ca^{2+} signal (red) and the predicted Ca^{2+} signal (green). The yellow arrow indicates a predicted Ca^{2+} spark. In close proximity to the predicted Ca^{2+} spark ground truth Ca^{2+} sparks can be observed. Predicted and ground truth Ca^{2+} sparks overlap partly sometimes. This fiber was unseen during the training process (Exp 1). Scale bar 10 μm **b**, Image sequence of another fiber. Other measurements of this fiber and this plane were seen during the training process (Exp 3). The yellow arrow indicates a predicted Ca^{2+} spark (green) that is close to several ground truth Ca^{2+} sparks (red) and on several images they partly overlap. The green arrow shows at a predicted Ca^{2+} spark that is not in close proximity to ground truth signals. The red arrow indicates a ground truth Ca^{2+} spark that is not in close proximity to predicted Ca^{2+} sparks. Scale bar 10 μm. **c** and **d**, xyt volumes of the measurements partly shown as image sequences in **a** and **b**. Yellow arrows indicate predicted Ca^{2+} sparks in close proximity to many ground truth Ca^{2+} sparks partly overlapping with them. Red arrows show at ground truth Ca^{2+} sparks with no corresponding predicted Ca^{2+} sparks at this location. Green arrow shows at predicted Ca^{2+} sparks with no corresponding ground truth Ca^{2+} sparks at this location. Box volume 34.88 μm, 34.88 μm, 122.18 s in **c** and 34.88 μm, 34.88 μm, 40.18 s in **d**. **e**, Pearson correlation coefficients of the whole images (light blue) and of the overlapping fiber masks of predicted and ground truth images (dark blue) for the three experiments. **f** and **g**, Matthews correlation coefficients and F1 scores calculated based on binary images of ground truth Ca^{2+} sparks and predicted Ca^{2+} sparks for the three experiments.

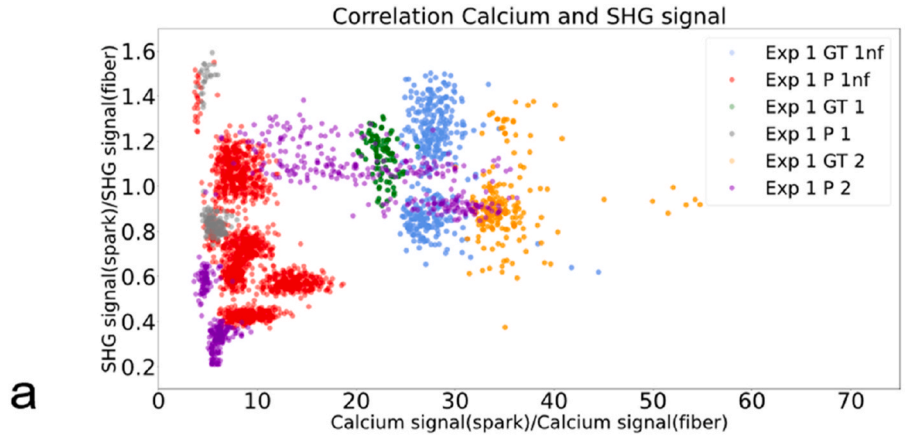

a

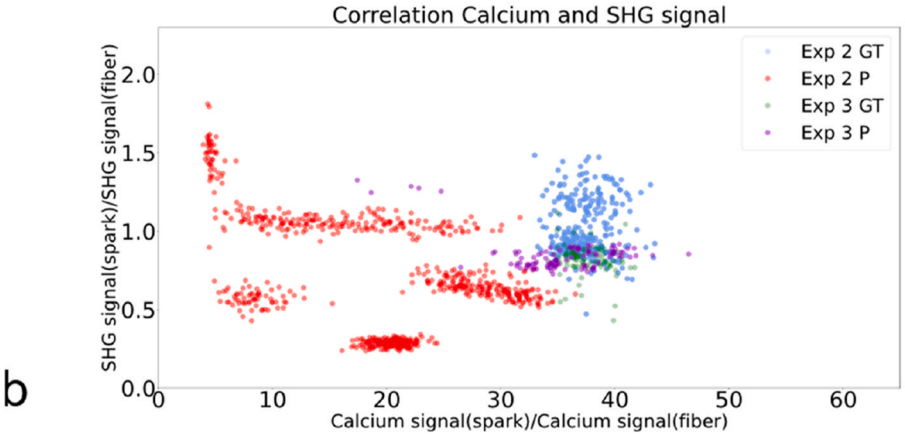

b

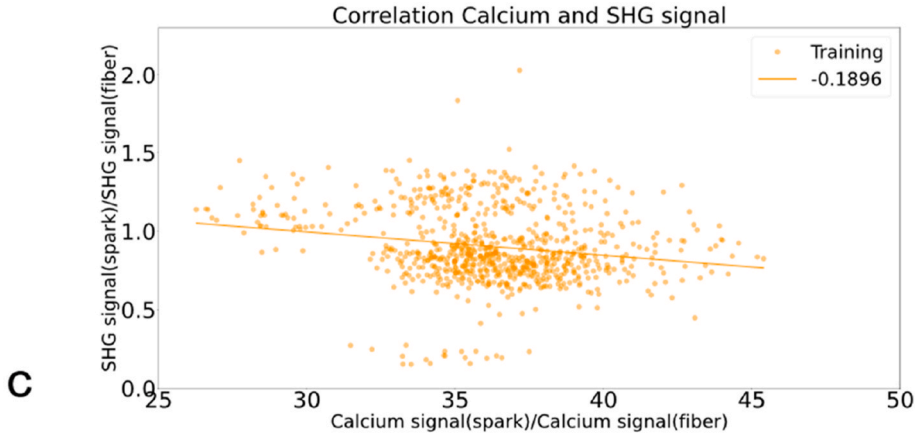

c

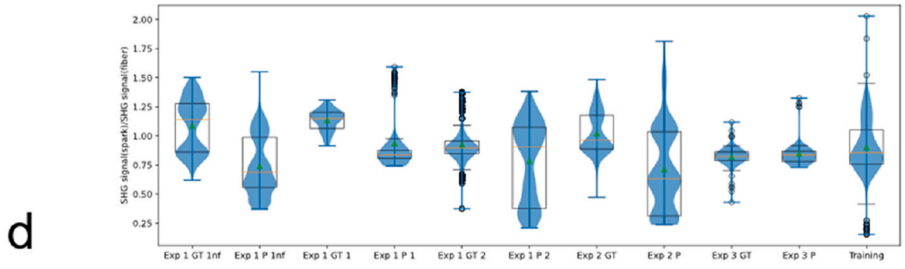

d

(caption on next page)

Fig. 5. Does the algorithm translate subcellular signals to subcellular signals? Correlation of the mean SHG signal and Ca^{2+} signal at Ca^{2+} sparks divided by the mean SHG signal and the Ca^{2+} signal of the fiber, when regions of Ca^{2+} sparks were excluded from the fiber mask, for the three experiments (**a** and **b**) and the training data set (**c**). Exp1 (Experiment 1) fiber 1 was measured without a band pass filter in front of the SHG signal detector (Exp 1 GT 1nf and Exp 1 P nf (ground truth and predicted data)), another measurement of fiber 1 (Exp 1) was carried out with a band pass filter in front of the SHG signal detector (Exp 1 GT 1 and Exp 1 P 1 (ground truth and predicted data)). Exp 1 GT 2 and Exp 1 P 2 are ground truth and predicted data of fiber 2 of Exp 1. Exp 2 GT and Exp 2 P and Exp 3 GT and Exp 3 P are ground truth and predicted data of Experiment 2 and 3. A linear regression is shown in **c** and the Pearson correlation coefficient is −0.1896 for the training data set. d Box plots and violin plots of the mean SHG signal at the region of a Ca^{2+} spark divided by the mean SHG signal of the fiber mask when regions of Ca^{2+} sparks were excluded from the fiber mask. Orange lines are the medians of the data and green triangles are the means.

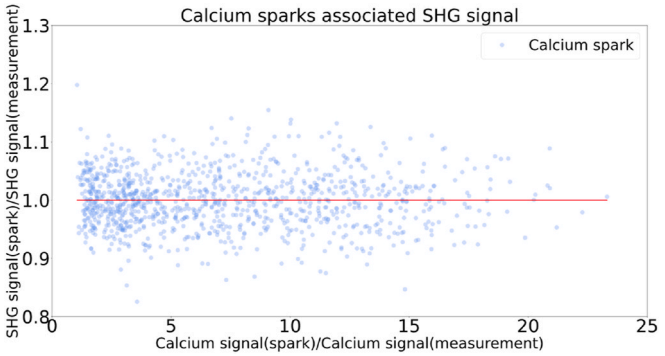

Fig. 6. SHG signal changes associated with Ca^{2+} sparks Ratios of SHG signal or Ca^{2+} signal at Ca^{2+} sparks and the mean SHG signal or the mean Ca^{2+} signal of the measurement (49 or 50 images) at the Ca^{2+} spark. Red line: Ratio SHG signal (spark)/SHG signal (measurement) of 1.

predicted data. The ratio SHG signal (spark)/SHG signal (fiber) is smaller for Exp 1 P 1nf compared to Exp 1 GT 1nf (Fig. 5d). The Ca^{2+} spark amplitude for the different experiments is shown in Extended Data Fig. 10.

The F1 score for the fiber masks in Exp 1 c1nf (cell 1 without a band pass filter) is somewhat lower than the F1 score in Exp 1 c1 and Exp 1 c2 (Extended Data Fig. 11). The F1 score for Ca^{2+} sparks is highest in Exp 1c1nf (Extended Data Fig. 11).

I investigated if the SHG signal at Ca^{2+} sparks changes compared to the mean SHG signal of the measurement at the same Ca^{2+} sparks. 53.46 % of Ca^{2+} sparks increased the SHG signal ratio>1 (1070 Ca^{2+} sparks, two mice, four fibers, ground truth data) (Fig. 6). The mean SHG signal ratio of Ca^{2+} sparks is not significantly changed 0.9996 ± 0.0014 (mean ± sem).

4. Discussion

Several properties of Ca^{2+} signals predicted based on label-free SHG measurements were in good agreement with the ground truth Ca^{2+} signals. Predictions of fast subcellular signals based on measurements of label-free techniques have the potential to replace staining of cells in some cases. The frequency of Ca^{2+} sparks, the fiber area and the Ca^{2+} spark area (in Exp 1) could be predicted quite well. Ca^{2+} sparks at myosin free regions might be nuclear Ca^{2+} sparks [54]. The poor prediction of Ca^{2+} sparks in Exp 2 suggests that a different plane of the same fiber is already a different scene with different myosin pattern and associated Ca^{2+} sparks signalling pattern. As expected, most predicted Ca^{2+} sparks were located at the fiber periphery. Small fiber shifts in part of the measurements might cause some inaccuracy in the analysis of Ca^{2+} sparks associated with y-shaped structures and the analysis of spark area over myosin filaments. The predicted Ca^{2+} spark frequency at y-shaped structures in Exp 3 is higher than the ground truth. In Exp 2 the predicted Ca^{2+} spark frequency at y-shaped structures is lower than the ground truth. This shows that the model has some limitations when predicting Ca^{2+} signals based on specific myosin patterns. Another reason might be that the data sets of Exp 2 and Exp 3 are smaller than the data set of Exp 1. Additionally, the mean of the ratio of SHG mean intensity at y-shaped structures and SHG mean intensity of the fiber based on the Ca^{2+} signal fiber mask was somewhat larger and SD somewhat smaller in Exp 3 compared to Exp 1 and Exp 2. This might be one reason for an overestimation. The fiber plane shown in Exp 2 is at the periphery of the fiber with a high frequency of Ca^{2+} sparks. It might be difficult to predict the Ca^{2+} signalling pattern based on a specific myosin filament pattern at the periphery of the fiber in Exp 2 with the training data set used here. The Ca^{2+} sparks frequency at y-shaped structures is lower in Exp 2 GT compared to Exp 1 GT and Exp 3 GT. In contrast, Exp 3 GT has the highest Ca^{2+} frequency at y-shaped structures of the ground truth data. Therefore, differences in image quality and specific properties of the myosin filament pattern might explain such underestimation and overestimation of the Ca^{2+} spark frequency at y-shaped structures. Ground truth and predicted data might be closer when analysed image-wise since the algorithm translates 2D images and not 3D images. This is particularly evident for the Ca^{2+} spark frequency at y-shaped structures in Exp 1.

Predicted Ca^{2+} sparks seen in all images of a measurement were in several cases associated with locations of high ground truth Ca^{2+} sparks activity.

The better F1 scores for Ca^{2+} sparks in Exp 1 1nf compared to Exp 1 1 (Extended Data Fig. 11) might be explained by a different part of the fiber that is easier to predict. The influence of a different plane for the prediction of Ca^{2+} sparks has been shown in Exp 2.

Although the training data shows a negative Pearson correlation, I think that results in Fig. 5 suggest that the algorithm translates mainly subcellular structures to subcellular signals and not subcellular signals to subcellular signals. Exp 1 GT 2 and Exp 2 GT show somewhat positive Pearson correlation (Fig. 5) in contrast to the training data, Exp 1 GT 1 and Exp 3 GT with a negative Pearson correlation. Additionally, a low SHG signal at Ca^{2+} sparks might be explained by specific positions within the fiber (perinuclear, nuclear signals or signals at the periphery of the fiber). The Pearson correlation coefficients of the predictions are negative for all experiments except Exp 1 P 2. Some Ca^{2+} sparks in skeletal muscle fibers might not be sufficient to increase the SHG signal as it was observed after a Ca^{2+} transient in skeletal muscle fibers [35]. Increased SHG signal has been observed for some sparks in the measurements presented here. But this needs further investigation and more sensitive optical systems might be able to measure Ca^{2+} sparks associated subcellular SHG signals more frequently. Measurements at most sensitive angles of relative laser polarization (0° and 180°) [34] will facilitate the detection of such SHG signal changes. Ca^{2+} sparks, short release events [55], (38.9 ± 1 ms) [4] and Ca^{2+} bursts, events with extended openings [55], (394.9 ± 26.7 ms) [4] were described in skeletal muscle fibers after hypotonic treatment [4]. However, localized Ca^{2+} signals lasting more than a second have been described after osmotic treatment in skeletal muscle fibers [54,55]. Better temporal resolution of the optical system will further improve the prediction of fast localized Ca^{2+} signals.

Predictions of localized Ca^{2+} signals might be more precise in cardiac muscle cells since local sarcomere contractions associated with Ca^{2+} sparks have been described in SHG measurements in a previous study [27]. Local changes in the sarcomere length as described in cardiac muscle cells [27] may be an important information for the algorithm. However, I did not investigate such local changes in the sarcomere length. Additionally, polarization dependent effects of the SHG signal [33–35] might influence the decision of the algorithm.

The SHG signal of myosin filaments used in this study was measured

in the forward direction. This approach has limitations and two objectives are needed. Although the SHG signal of myosin filaments is stronger in the forward direction [25], SHG signals were also measured *in vivo* in the backward direction previously [25]. Similar predictions of Ca^{2+} signals based on the SHG signal of myosin filaments might be carried out for *in vivo* SHG measurements of myosin filaments in the backward direction after an appropriate training.

In principle this technique can be extended to other label-free microscopy techniques and other fluorescent indicators such as dopamine [56–59], acetylcholine [60,61], glutamate [62,63], GABA [64], ATP [12,65], serotonin [66], norepinephrine [67] and adenosine [68] indicators.

The prediction of the exact location of Ca^{2+} sparks based on subcellular structures remains a difficult task. In further improvement of the algorithm the 3D nature of xyt volumes should be taken into account instead of translating 2D images. Other existing algorithms such as U-net [69] could be tested for such a task as it was done in an image translation study of medical images [21]. It can be expected that data augmentation of the training data set [12,69,70], pre-processing of the SHG signal, denoising, larger data sets, powerful computational resources and algorithms designed for this specific task will further improve the accuracy of such image translations. Recent advances in super-resolution SHG techniques [71,72] might further improve the localization of Ca^{2+} sparks. Additionally, an improved resolution of the SHG measurements might provide new structural information and improve such predictions. In some cases and after further improvement of such predictions, label-free SHG measurements and a software similar to the one described in this manuscript might be used as a Ca^{2+} indicator in cardiac and skeletal muscle.

I hope that this work will stimulate further research to improve the translation of fast subcellular signals based on subcellular structures or other subcellular signals.

Ethics statement

This research does not need an Ethics statement because ground truth data is already published (measurements of mouse skeletal muscle fibers).

Code availability

The code and the checkpoint used in this paper are provided at https://github.com/TihomirGeorgiev3/SHGtoSpark_part_1 and https://github.com/TihomirGeorgiev3/SHGtoSpark_part_2.

Declaration of competing interest

The authors declare that they have no known competing financial interests or personal relationships that could have appeared to influence the work reported in this paper.

Appendix A. Supplementary data

Supplementary data to this article can be found online at https://doi.org/10.1016/j.compbiomed.2025.111138.

Data availability

Data will be provided upon request. Some images are provided at https://github.com/TihomirGeorgiev3/SHGtoSpark_part_1 and https://github.com/TihomirGeorgiev3/SHGtoSpark_part_2. The algorithms can be tested on these images.

References

[1] M.J. Berridge, M.D. Bootman, H.L. Roderick, Calcium signalling: dynamics, homeostasis and remodelling, Nat. Rev. Mol. Cell Biol. 4 (7) (2003) 517–529, https://doi.org/10.1038/nrm1155. PubMed PMID: 12838335.

[2] H. Cheng, W.J. Lederer, M.B. Cannell, Calcium sparks: elementary events underlying excitation-contraction coupling in heart muscle, Science 262 (5134) (1993) 740–744, https://doi.org/10.1126/science.8235594. PubMed PMID: 8235594.

[3] H. Cheng, W.J. Lederer, Calcium sparks, Physiol. Rev. 88 (4) (2008) 1491–1545, https://doi.org/10.1152/physrev.00030.2007. PubMed PMID: 18923188.

[4] X. Wang, N. Weisleder, C. Collet, J. Zhou, Y. Chu, Y. Hirata, et al., Uncontrolled calcium sparks act as a dystrophic signal for Mammalian skeletal muscle, Nat. Cell Biol. 7 (5) (2005) 525–530, https://doi.org/10.1038/ncb1254. Epub 20050417. PubMed PMID: 15834406.

[5] W.G. Kirsch, D. Uttenweiler, R.H. Fink, Spark- and ember-like elementary Ca2+ release events in skinned fibres of adult mammalian skeletal muscle, J. Physiol. 537 (Pt 2) (2001) 379–389, https://doi.org/10.1111/j.1469-7793.2001.00379.x. PubMed PMID: 11731572; PubMed Central PMCID: PMCPMC2278952.

[6] L. Theis, P. Berens, E. Froudarakis, J. Reimer, M. Roman Roson, T. Baden, et al., Benchmarking spike rate inference in population calcium imaging, Neuron 90 (3) (2016) 471–482, https://doi.org/10.1016/j.neuron.2016.04.014. PubMed PMID: 27151639; PubMed Central PMCID: PMCPMC4888799.

[7] P. Berens, J. Freeman, T. Deneux, N. Chenkov, T. McColgan, A. Speiser, et al., Community-based benchmarking improves spike rate inference from two-photon calcium imaging data, PLoS Comput. Biol. 14 (5) (2018) e1006157, https://doi.org/10.1371/journal.pcbi.1006157. Epub 20180521, PubMed PMID: 29782491; PubMed Central PMCID: PMCPMC5997358.

[8] X. Li, G. Zhang, J. Wu, Y. Zhang, Z. Zhao, X. Lin, et al., Reinforcing neuron extraction and spike inference in calcium imaging using deep self-supervised denoising, Nat. Methods 18 (11) (2021) 1395–1400, https://doi.org/10.1038/s41592-021-01225-0. Epub 20210816, PubMed PMID: 34400836.

[9] P. Rupprecht, S. Carta, A. Hoffmann, M. Echizen, A. Blot, A.C. Kwan, et al., A database and deep learning toolbox for noise-optimized, generalized spike inference from calcium imaging, Nat. Neurosci. 24 (9) (2021) 1324–1337, https://doi.org/10.1038/s41593-021-00895-5. Epub 20210802, PubMed PMID: 34341584; PubMed Central PMCID: PMCPMC7611618.

[10] J. Lecoq, M. Oliver, J.H. Siegle, N. Orlova, P. Ledochowitsch, C. Koch, Removing independent noise in systems neuroscience data using DeepInterpolation, Nat. Methods 18 (11) (2021) 1401–1408, https://doi.org/10.1038/s41592-021-01285-2. Epub 20211014, PubMed PMID: 34650233; PubMed Central PMCID: PMCPMC8833814.

[11] L. Sita, M. Brondi, P. Lagomarsino de Leon Roig, S. Curreli, M. Panniello, D. Vecchia, et al., A deep-learning approach for online cell identification and trace extraction in functional two-photon calcium imaging, Nat. Commun. 13 (1) (2022) 1529, https://doi.org/10.1038/s41467-022-29180-0. Epub 20220322, PubMed PMID: 35318335; PubMed Central PMCID: PMCPMC8940911.

[12] X. Li, Y. Li, Y. Zhou, J. Wu, Z. Zhao, J. Fan, et al., Real-time denoising enables high-sensitivity fluorescence time-lapse imaging beyond the shot-noise limit, Nat. Biotechnol. 41 (2) (2023) 282–292, https://doi.org/10.1038/s41587-022-01450-8. Epub 20220926, PubMed PMID: 36163547; PubMed Central PMCID: PMCPMC9931589.

[13] I. Goodfellow, J. Pouget-Abadie, M. Mirza, B. Xu, D. Warde-Farley, S. Ozair, et al., Generative adversarial nets, Adv. Neural Inf. Process. Syst. 27 (2014).

[14] S.A. Kamran, K.F. Hossain, H. Moghnieh, S. Riar, A. Bartlett, A. Tavakkoli, et al., New open-source software for subcellular segmentation and analysis of spatiotemporal fluorescence signals using deep learning, iScience 25 (5) (2022) 104277, https://doi.org/10.1016/j.isci.2022.104277. Epub 20220421, PubMed PMID: 35573197; PubMed Central PMCID: PMCPMC9095751.

[15] S. Yang, R. Li, J. Chen, Z. Li, Z. Huang, W. Xie, Calcium spark detection and event-based classification of single cardiomyocyte using deep learning, Front. Physiol. 12 (2021) 770051, https://doi.org/10.3389/fphys.2021.770051. Epub 20211108, PubMed PMID: 34819876; PubMed Central PMCID: PMCPMC8607692.

[16] R. Janicek, H. Agarwal, A.M. Gomez, M. Egger, G.C.R. Ellis-Davies, E. Niggli, Local recovery of cardiac calcium-induced calcium release interrogated by ultra-effective, two-photon uncaging of calcium, J. Physiol. 599 (16) (2021) 3841–3852, https://doi.org/10.1113/JP281482. Epub 20210802, PubMed PMID: 34245001; PubMed Central PMCID: PMCPMC8456848.

[17] P. Dotti, M. Fernandez-Tenorio, R. Janicek, P. Marquez-Neila, M. Wullschleger, R. Sznitman, et al., A deep learning-based approach for efficient detection and classification of local Ca(2)(+) release events in Full-Frame confocal imaging, Cell Calcium 121 (2024) 102893, https://doi.org/10.1016/j.ceca.2024.102893. Epub 20240424, PubMed PMID: 38701707.

[18] S. This, S. Costantino, H.J. Melichar, Machine learning predictions of T cell antigen specificity from intracellular calcium dynamics, Sci. Adv. 10 (10) (2024) eadk2298, https://doi.org/10.1126/sciadv.adk2298. Epub 20240306, PubMed PMID: 38446885; PubMed Central PMCID: PMCPMC10917351.

[19] E.M. Christiansen, S.J. Yang, D.M. Ando, A. Javaherian, G. Skibinski, S. Lipnick, et al., In silico labeling: predicting fluorescent labels in unlabeled images, Cell 173 (3) (2018) 792–803 e19, https://doi.org/10.1016/j.cell.2018.03.040. Epub 20180412, PubMed PMID: 29656897; PubMed Central PMCID: PMCPMC6309178.

[20] C. Ounkomol, S. Seshamani, M.M. Maleckar, F. Collman, G.R. Johnson, Label-free prediction of three-dimensional fluorescence images from transmitted-light microscopy, Nat. Methods 15 (11) (2018) 917–920, https://doi.org/10.1038/s41592-018-0111-2. Epub 20180917, PubMed PMID: 30224672; PubMed Central PMCID: PMCPMC6212323.

[21] C. Jayachandran Preetha, H. Meredig, G. Brugnara, M.A. Mahmutoglu, M. Foltyn, F. Isensee, et al., Deep-learning-based synthesis of post-contrast T1-weighted MRI for tumour response assessment in neuro-oncology: a multicentre, retrospective cohort study, Lancet Digit. Health 3 (12) (2021) e784–e794, https://doi.org/10.1016/S2589-7500(21)00205-3. Epub 20211020, PubMed PMID: 34688602.
[22] Generation of amyloid PET images via conditional adversarial training for predicting progression to Alzheimer's Disease, in: Y. Yan, H. Lee, E. Somer, V. Grau (Eds.), Predictive Intelligence in Medicine, Springer International Publishing, Cham, 2018, 2018.
[23] M. Both, M. Vogel, O. Friedrich, F. von Wegner, T. Kunsting, R.H. Fink, et al., Second harmonic imaging of intrinsic signals in muscle fibers in situ, J. Biomed. Opt. 9 (5) (2004) 882–892, https://doi.org/10.1117/1.1783354. PubMed PMID: 15447009.
[24] S.V. Plotnikov, A.C. Millard, P.J. Campagnola, W.A. Mohler, Characterization of the myosin-based source for second-harmonic generation from muscle sarcomeres, Biophys. J. 90 (2) (2006) 693–703, https://doi.org/10.1529/biophysj.105.071555. Epub 20051028, PubMed PMID: 16258040; PubMed Central PMCID: PMCPMC1367074.
[25] M.E. Llewellyn, R.P. Barretto, S.L. Delp, M.J. Schnitzer, Minimally invasive high-speed imaging of sarcomere contractile dynamics in mice and humans, Nature 454 (7205) (2008) 784–788, https://doi.org/10.1038/nature07104. Epub 20080706, PubMed PMID: 18600262; PubMed Central PMCID: PMCPMC2826360.
[26] T. Georgiev, B. Zapiec, M. Forderer, R.H.A. Fink, M. Vogel, Colocalization properties of elementary Ca(2+) release signals with structures specific to the contractile filaments and the tubular system of intact mouse skeletal muscle fibers, J. Struct. Biol. 192 (3) (2015) 366–375, https://doi.org/10.1016/j.jsb.2015.09.018. Epub 20151021, PubMed PMID: 26431893.
[27] S. Awasthi, L.T. Izu, Z. Mao, Z. Jian, T. Landas, A. Lerner, et al., Multimodal SHG-2PF imaging of microdomain Ca2+-Contraction coupling in live cardiac myocytes, Circ. Res. 118 (2) (2016) e19–e28, https://doi.org/10.1161/CIRCRESAHA.115.307919. Epub 20151207, PubMed PMID: 26643875; PubMed Central PMCID: PMCPMC4740258.
[28] W. Denk, J.H. Strickler, W.W. Webb, Two-photon laser scanning fluorescence microscopy, Science 248 (4951) (1990) 73–76, https://doi.org/10.1126/science.2321027. PubMed PMID: 2321027.
[29] L.A. Gatys, A.S. Ecker, M. Bethge, A neural algorithm of artistic style, CoRR (2015). https://arxiv.org/abs/1508.06576.
[30] P. Isola, J.- Zhu, Yan, T. Zhou, A.A. Efros, Image-to-Image translation with conditional adversarial networks, CoRR (2016) 07004 abs/1611.
[31] O. Friedrich, M. Both, C. Weber, S. Schurmann, M.D. Teichmann, F. von Wegner, et al., Microarchitecture is severely compromised but motor protein function is preserved in dystrophic mdx skeletal muscle, Biophys. J. 98 (4) (2010) 606–616, https://doi.org/10.1016/j.bpj.2009.11.005. PubMed PMID: 20159157; PubMed Central PMCID: PMCPMC2820646.
[32] M.D. Teichmann, F.V. Wegner, R.H. Fink, J.S. Chamberlain, B.S. Launikonis, B. Martinac, et al., Inhibitory control over Ca(2+) sparks via mechanosensitive channels is disrupted in dystrophin deficient muscle but restored by mini-dystrophin expression, PLoS One 3 (11) (2008) e3644, https://doi.org/10.1371/journal.pone.0003644. Epub 20081104, PubMed PMID: 18982068; PubMed Central PMCID: PMCPMC2575405.
[33] V. Nucciotti, C. Stringari, L. Sacconi, F. Vanzi, L. Fusi, M. Linari, et al., Probing myosin structural conformation in vivo by second-harmonic generation microscopy, Proc. Natl. Acad. Sci. U. S. A. 107 (17) (2010) 7763–7768, https://doi.org/10.1073/pnas.0914782107. Epub 20100412, PubMed PMID: 20385845; PubMed Central PMCID: PMCPMC2867856.
[34] S. Schurmann, F. von Wegner, R.H. Fink, O. Friedrich, M. Vogel, Second harmonic generation microscopy probes different states of motor protein interaction in myofibrils, Biophys. J. 99 (6) (2010) 1842–1851, https://doi.org/10.1016/j.bpj.2010.07.005. PubMed PMID: 20858429; PubMed Central PMCID: PMCPMC2941014.
[35] M. Forderer, T. Georgiev, M. Mosqueira, R.H. Fink, M. Vogel, Functional second harmonic generation microscopy probes molecular dynamics with high temporal resolution, Biomed. Opt. Express 7 (2) (2016) 525–541, https://doi.org/10.1364/BOE.7.000525. Epub 20160115, PubMed PMID: 26977360; PubMed Central PMCID: PMCPMC4771469.
[36] O. Friedrich, T. Ehmer, R.H. Fink, Calcium currents during contraction and shortening in enzymatically isolated murine skeletal muscle fibres, J. Physiol. 517 (Pt 3) (1999) 757–770, https://doi.org/10.1111/j.1469-7793.1999.0757s.x. PubMed PMID: 10358116; PubMed Central PMCID: PMCPMC2269387.
[37] G. Brum, A. González, J. Rengifo, N. Shirokova, E. Ríos, Fast imaging in two dimensions resolves extensive sources of Ca2+ sparks in frog skeletal muscle, J. Physiol. 528 (Pt 3) (2000) 419–433, https://doi.org/10.1111/j.1469-7793.2000.00419.x. PubMed PMID: 11060121; PubMed Central PMCID: PMCPMC2270146.
[38] E.M. Steele, D.S. Steele, Automated detection and analysis of Ca(2+) sparks in x-y image stacks using a thresholding algorithm implemented within the open-source image analysis platform ImageJ, Biophys. J. 106 (3) (2014) 566–576, https://doi.org/10.1016/j.bpj.2013.12.040. PubMed PMID: 24507597; PubMed Central PMCID: PMCPMC3944640.
[39] J. Schindelin, I. Arganda-Carreras, E. Frise, V. Kaynig, M. Longair, T. Pietzsch, et al., Fiji: an open-source platform for biological-image analysis, Nat. Methods 9 (7) (2012) 676–682, https://doi.org/10.1038/nmeth.2019. Epub 2012/06/30, PubMed PMID: 22743772; PubMed Central PMCID: PMCPMC3855844.
[40] P. Virtanen, R. Gommers, T.E. Oliphant, M. Haberland, T. Reddy, D. Cournapeau, et al., SciPy 1.0: fundamental algorithms for scientific computing in Python, Nat. Methods 17 (3) (2020) 261–272, https://doi.org/10.1038/s41592-019-0686-2. Epub 2020/02/06, PubMed PMID: 32015543; PubMed Central PMCID: PMCPMC7056644.
[41] F. Pedregosa, Ge Varoquaux, A. Gramfort, V. Michel, B. Thirion, O. Grisel, et al., Scikit-learn: machine learning in python, J. Mach. Learn. Res. 12 (85) (2011) 2825–2830.
[42] Z. Wang, A.C. Bovik, H.R. Sheikh, E.P. Simoncelli, Image quality assessment: from error visibility to structural similarity, IEEE Trans. Image Process. 13 (4) (2004) 600–612.
[43] Z. Wang, A.C. Bovik, Mean squared error: love it or leave it? A new look at Signal fidelity measures, IEEE Signal Process. Mag. 26 (1) (2009) 98–117.
[44] S. van der Walt, J.L. Schonberger, J. Nunez-Iglesias, F. Boulogne, J.D. Warner, N. Yager, et al., scikit-image: image processing in Python, PeerJ 2 (2014) e453, https://doi.org/10.7717/peerj.453. Epub 2014/07/16, PubMed PMID: 25024921; PubMed Central PMCID: PMCPMC4081273.
[45] J.D. Hunter, Matplotlib: a 2D graphics environment, Comput. Sci. Eng. (2007), https://doi.org/10.1109/MCSE.2007.55.
[46] E. Moen, D. Bannon, T. Kudo, W. Graf, M. Covert, D. Van Valen, Deep learning for cellular image analysis, Nat. Methods 16 (12) (2019) 1233–1246, https://doi.org/10.1038/s41592-019-0403-1. Epub 2019/05/28, PubMed PMID: 31133758; PubMed Central PMCID: PMCPMC8759575.
[47] M. Abadi, A. Agarwal, P. Barham, E. Brevdo, Z. Chen, C. Citro, et al., Tensorflow: Large-Scale Machine Learning on Heterogeneous Systems, 2015, https://doi.org/10.5281/zenodo.7764425.
[48] F. Chollet, Others. Keras, 2015.
[49] C.R. Harris, K.J. Millman, S.J. van der Walt, R. Gommers, P. Virtanen, D. Cournapeau, et al., Array programming with NumPy, Nature 585 (7825) (2020) 357–362, https://doi.org/10.1038/s41586-020-2649-2. Epub 2020/09/18, PubMed PMID: 32939066; PubMed Central PMCID: PMCPMC7759461.
[50] C. Gohlke, Tifffile, 2022, https://doi.org/10.5281/zenodo.6795861.
[51] F. Perez, B.E. Granger, IPython: a System for interactive scientific computing, Comput. Sci. Eng. 9 (3) (2007) 21–29.
[52] C.A. Schneider, W.S. Rasband, K.W. Eliceiri, NIH image to ImageJ: 25 years of image analysis, Nat. Methods 9 (7) (2012) 671–675, https://doi.org/10.1038/nmeth.2089. Epub 2012/08/30, PubMed PMID: 22930834; PubMed Central PMCID: PMCPMC5554542.
[53] E.F. Pettersen, T.D. Goddard, C.C. Huang, E.C. Meng, G.S. Couch, T.I. Croll, et al., UCSF ChimeraX: structure visualization for researchers, educators, and developers, Protein Sci. 30 (1) (2021) 70–82, https://doi.org/10.1002/pro.3943. Epub 2020/09/04, PubMed PMID: 32881101; PubMed Central PMCID: PMCPMC7737788.
[54] T. Georgiev, M. Svirin, E. Jaimovich, R.H. Fink, Localized nuclear and perinuclear Ca(2+) signals in intact mouse skeletal muscle fibers, Front. Physiol. 6 (2015) 263, https://doi.org/10.3389/fphys.2015.00263. Epub 20150929, PubMed PMID: 26483696; PubMed Central PMCID: PMCPMC4586431.
[55] N. Weisleder, J.J. Ma, Ca2+ sparks as a plastic signal for skeletal muscle health, aging, and dystrophy, Acta Pharmacol. Sin. 27 (7) (2006) 791–798, https://doi.org/10.1111/j.1745-7254.2006.00384.x. PubMed PMID: 16787561.
[56] F. Sun, J. Zeng, M. Jing, J. Zhou, J. Feng, S.F. Owen, et al., A genetically encoded fluorescent sensor enables rapid and specific detection of dopamine in flies, fish, and mice, Cell 174 (2) (2018) 481–96 e19, https://doi.org/10.1016/j.cell.2018.06.042. PubMed PMID: 30007419; PubMed Central PMCID: PMCPMC6092020.
[57] T. Patriarchi, J.R. Cho, K. Merten, M.W. Howe, A. Marley, W.H. Xiong, et al., Ultrafast neuronal imaging of dopamine dynamics with designed genetically encoded sensors, Science 360 (6396) (2018), https://doi.org/10.1126/science.aat4422. Epub 20180531, PubMed PMID: 29853555; PubMed Central PMCID: PMCPMC6287765.
[58] T. Patriarchi, A. Mohebi, J. Sun, A. Marley, R. Liang, C. Dong, et al., An expanded palette of dopamine sensors for multiplex imaging in vivo, Nat. Methods 17 (11) (2020) 1147–1155, https://doi.org/10.1038/s41592-020-0936-3. Epub 20200907, PubMed PMID: 32895537; PubMed Central PMCID: PMCPMC8169200.
[59] F. Sun, J. Zhou, B. Dai, T. Qian, J. Zeng, X. Li, et al., Next-generation GRAB sensors for monitoring dopaminergic activity in vivo, Nat. Methods 17 (11) (2020) 1156–1166, https://doi.org/10.1038/s41592-020-00981-9. Epub 20201021, PubMed PMID: 33087905; PubMed Central PMCID: PMCPMC7648260.
[60] M. Jing, P. Zhang, G. Wang, J. Feng, L. Mesik, J. Zeng, et al., A genetically encoded fluorescent acetylcholine indicator for in vitro and in vivo studies, Nat. Biotechnol. 36 (8) (2018) 726–737, https://doi.org/10.1038/nbt.4184. Epub 20180709, PubMed PMID: 29985477; PubMed Central PMCID: PMCPMC6093211.
[61] M. Jing, Y. Li, J. Zeng, P. Huang, M. Skirzewski, O. Kljakic, et al., An optimized acetylcholine sensor for monitoring in vivo cholinergic activity, Nat. Methods 17 (11) (2020) 1139–1146, https://doi.org/10.1038/s41592-020-0953-2. Epub 20200928, PubMed PMID: 32989318; PubMed Central PMCID: PMCPMC7606762.
[62] N. Helassa, C.D. Durst, C. Coates, S. Kerruth, U. Arif, C. Schulze, et al., Ultrafast glutamate sensors resolve high-frequency release at Schaffer collateral synapses, Proc. Natl. Acad. Sci. U. S. A 115 (21) (2018) 5594–5599, https://doi.org/10.1073/pnas.1720648115. Epub 20180507, PubMed PMID: 29735711; PubMed Central PMCID: PMCPMC6003469.
[63] J.S. Marvin, B. Scholl, D.E. Wilson, K. Podgorski, A. Kazemipour, J.A. Muller, et al., Stability, affinity, and chromatic variants of the glutamate sensor iGluSnFR, Nat. Methods 15 (11) (2018) 936–939, https://doi.org/10.1038/s41592-018-0171-3. Epub 20181030, PubMed PMID: 30377363; PubMed Central PMCID: PMCPMC6394230.
[64] J.S. Marvin, Y. Shimoda, V. Magloire, M. Leite, T. Kawashima, T.P. Jensen, et al., A genetically encoded fluorescent sensor for in vivo imaging of GABA, Nat. Methods 16 (8) (2019) 763–770, https://doi.org/10.1038/s41592-019-0471-2. Epub 20190715, PubMed PMID: 31308547.

[65] Z. Wu, K. He, Y. Chen, H. Li, S. Pan, B. Li, et al., A sensitive GRAB sensor for detecting extracellular ATP in vitro and in vivo, Neuron 110 (5) (2022) 770–782 e5, https://doi.org/10.1016/j.neuron.2021.11.027. Epub 20211222, PubMed PMID: 34942116.

[66] J. Wan, W. Peng, X. Li, T. Qian, K. Song, J. Zeng, et al., A genetically encoded sensor for measuring serotonin dynamics, Nat. Neurosci. 24 (5) (2021) 746–752, https://doi.org/10.1038/s41593-021-00823-7. Epub 20210405, PubMed PMID: 33821000; PubMed Central PMCID: PMCPMC8544647.

[67] J. Feng, C. Zhang, J.E. Lischinsky, M. Jing, J. Zhou, H. Wang, et al., A genetically encoded fluorescent sensor for rapid and specific in vivo detection of norepinephrine, Neuron 102 (4) (2019) 745–761 e8, https://doi.org/10.1016/j.neuron.2019.02.037. Epub 20190325, PubMed PMID: 30922875; PubMed Central PMCID: PMCPMC6533151.

[68] W. Peng, Z. Wu, K. Song, S. Zhang, Y. Li, M. Xu, Regulation of sleep homeostasis mediator adenosine by basal forebrain glutamatergic neurons, Science 369 (6508) (2020), https://doi.org/10.1126/science.abb0556. PubMed PMID: 32883833.

[69] U-Net: Convolutional networks for biomedical image segmentation, in: O. Ronneberger, P. Fischer, T. Brox (Eds.), Medical Image Computing and Computer-Assisted Intervention – MICCAI 2015, Springer International Publishing, Cham, 2015.

[70] A. Dosovitskiy, J.T. Springenberg, M. Riedmiller, T. Brox, Discriminative unsupervised feature learning with convolutional neural networks, Adv. Neural Inf. Process. Syst. 27 (2014).

[71] I. Gregor, M. Spiecker, R. Petrovsky, J. Grosshans, R. Ros, J. Enderlein, Rapid nonlinear image scanning microscopy, Nat. Methods 14 (11) (2017) 1087–1089, https://doi.org/10.1038/nmeth.4467. Epub 20171016, PubMed PMID: 29039418.

[72] S.G. Stanciu, R. Hristu, G.A. Stanciu, D.E. Tranca, L. Eftimie, A. Dumitru, et al., Super-resolution re-scan second harmonic generation microscopy, Proc. Natl. Acad. Sci. U. S. A 119 (47) (2022) e2214662119, https://doi.org/10.1073/pnas.2214662119. Epub 20221114, PubMed PMID: 36375085; PubMed Central PMCID: PMCPMC9704717.